

Chemical potential and magnetic field effects on graphene magnetoplasmons

Ningning Wang, Linhui Ding, and Weihua Wang ^{*}

School of Material Science and Physics, China University of Mining and Technology, Xuzhou 221116, People's Republic of China



(Received 15 March 2023; revised 19 June 2023; accepted 24 July 2023; published 3 August 2023)

Due to its strong magneto-optical response, plasmons in graphene can be actively tuned by a static magnetic field, resulting in another quasiparticle called graphene magnetoplasmon (GMP). In this work, we theoretically investigate GMPs in graphene disks with their two halves subject to two magnetic fields. As the two magnetic fields are identical (case I), the well-known symmetric mode splitting is observed for a larger chemical potential μ_c , with two GMPs (GMP_{\pm}) being circularly polarized with different chirality; with decreasing μ_c , the lower-energy GMP_{-} will become an edge mode with a significantly reduced damping rate. As the two magnetic fields are opposite (case II), the magnetic field effect is completely absent for a larger μ_c , e.g., GMP_{\pm} are degenerate and linear polarized, while for a smaller μ_c , GMP_{\pm} will be circularly polarized again, and GMP_{-} is circulating unidirectionally along the magnetic border. However, if two magnetic fields are different in magnitude, both GMP_{\pm} will exhibit field circulating along the border, and more interestingly, in the same direction as case II, namely, the opposite field circulating is prohibited. Having a small defect, the unidirectional field circulating is not broken, which will pass around the defect smoothly. Finally, we propose a feasible scheme, graphene folding, for producing specified magnetic fields, in which two halves of the disk are folded with different angles to a uniform magnetic field. In spite of structural deformation, the main features of GMP_{\pm} are shown to be well maintained. Our work provides a better understanding of magnetoplasmons in graphene, which could be of interest to plasmonic and magneto-optic device applications.

DOI: [10.1103/PhysRevB.108.085406](https://doi.org/10.1103/PhysRevB.108.085406)

I. INTRODUCTION

Plasmonic resonances, collective excitations of conduction electrons induced by electromagnetic waves, can enable light manipulation beyond the diffraction limit [1–3], and thus are intensively used in enhancing light-matter interactions at nanoscale [4–6]. Graphene, an emerging two-dimensional (2D) material, has recently been demonstrated to be a suitable alternative to noble metals for launching plasmons, so-called graphene plasmons [7–9]. They exhibit distinct advantages over conventional plasmons in many aspects, such as local field enhancement and confinement [10–12], intrinsic lifetime [13–15], terahertz (THz) and infrared operating frequencies [16–18], and most importantly, active tunability via external gating [19,20]. These achievements benefit from the unique features of low-energy charge carriers in graphene, which are 2D massless Dirac fermions with a linear energy dispersion [21–23]. Graphene plasmons can thereby serve as a promising platform for plasmon-enabled studies on, e.g., non-local optics [24–26], nonlinear optics [27–29], and quantum optics [30–32].

On the other hand, different from those common plasmonic materials (noble metals), graphene possesses strong magnetic field effect. The most direct evidence is the observations of room-temperature quantum Hall effect [33–35], which can only be observed in traditional 2D electron systems at nearly zero temperature. In the presence of magnetic field, the energy

of charge carriers in graphene is quantized into nonequidistant degenerate Landau levels [36–38]. Accordingly, the collective excitation of these carriers will be extremely modulated, with the quasiparticles mediated by cyclotron resonances, known as magnetoplasmons (MPs) [39–41], which combine magnetic and plasmonic functionalities. Hence, apart from electrostatic gating (electric field equivalently), magnetic field provides a new degree of freedom for controlling graphene MPs (GMPs). Meanwhile, GMPs have already been demonstrated to support giant magneto-optical Faraday rotation [42,43], topologically protected transportation [44–49], nonreciprocal isolation [50], Goos-Hanchen effect [51], Kerr effect [52], photonic spin Hall effect [53], and so on.

In finite structures, a well-known effect of MPs (as well as GMPs) is the mode splitting, with two induced states carrying left/right-hand circular polarization (L/RHCP), respectively. In some studies [54–56], the two states are demonstrated to be symmetrically distributed with respect to plasmon frequencies at zero magnetic field, with roughly identical damping rates, while in the other studies [57–59] the splitting is shown to be asymmetric, with the lower-frequency state having a smaller damping rate. In the latter case, the two states are classified as a bulk MP and an edge MP. Even though these two results are often observed, their differences and connections remain still not physically transparent, which might be more complicated in nonuniform magnetic fields.

In this work, we investigate GMPs in graphene disks with their two halves subject to two identical (uniform) or different magnetic fields, in particular, their evolution as a function of chemical potential and magnetic field. In a uniform magnetic

^{*}wh.wang@outlook.com

field, the well-known symmetric mode splitting is observed at larger chemical potential and smaller magnetic field, but with decreasing chemical potential or increasing magnetic field, it will evolve into an asymmetric mode splitting, with the edge GMP having an extremely reduced damping rate. In contrast, if two magnetic fields are opposite, we show two GMPs are degenerate and linearly polarized at larger chemical potential, and by reducing chemical potential, they will split and return to be circularly polarized. Interestingly, their field circulating will be bound to each half, which will cross the magnetic border for one GMP and is canceled for the other GMP. This feature can be well maintained even in the presence of a small defect. Finally, we propose folded graphene structures to achieve the studied magnetic field distributions and GMP excitations. Our findings bridge two fundamental effects of GMP splitting, and improve our understanding of unidirectional field circulating of GMPs.

II. OPTICAL RESPONSE OF GRAPHENE

As a typical 2D material, the optical response of graphene can be characterized macroscopically through its frequency-dependent surface conductivity $\sigma(\omega)$. In practice, $\sigma(\omega)$ can be derived within the framework of linear response theory by taking into account single-particle transitions of those Dirac fermions. Interestingly, at THz and infrared frequencies, the complicated expression of $\sigma(\omega)$ can be reduced to a simple Drude formula that is often used for noble metals [60–62]. In the presence of a magnetic field, the energy of Dirac fermions is quantized into nonequidistant Landau levels (LLs), including a zero-energy LL [63–65]. Accordingly, the magneto-optical response of graphene is determined directly by single-particle transitions between different LLs, while at the limit of high doping, the LLs around Fermi level play the key role. In this instance, the magneto-optical conductivity $\sigma(\omega)$ of graphene will have a similar formula as that of traditional 2D electron gases, yet with a Fermi-level dependent effective mass [63]. To carry out full-wave simulations, three-dimensional (3D) dielectric function $\varepsilon(\omega)$ is required. Herein, we also follow the common practice to model graphene as a very thin 3D film with an artificial thickness t_g (0.5 nm throughout this paper), and then the in-plane components $\varepsilon_{in}(\omega)$ of effective $\varepsilon(\omega)$ can be readily written as

$$\varepsilon_{in}(\omega) = \varepsilon_0 + \frac{i}{\omega t_g} \begin{bmatrix} \sigma_{xx}(\omega) & \sigma_{xy}(\omega) \\ \sigma_{yx}(\omega) & \sigma_{yy}(\omega) \end{bmatrix}, \quad (1)$$

while the out-plane diagonal term $\varepsilon_{zz} = \varepsilon_0$, and all the other off-diagonal terms are simply zero. The Drude formulas for the conductivity terms in brackets are given by [66,67]

$$\begin{aligned} \sigma_{xx}(\omega) = \sigma_{yy}(\omega) &= \frac{e^2 \mu_c}{\pi \hbar^2} \frac{i(\omega + i\tau^{-1})}{(\omega + i\tau^{-1})^2 - \omega_c^2}, \\ \sigma_{xy}(\omega) = -\sigma_{yx}(\omega) &= \frac{e^2 \mu_c}{\pi \hbar^2} \frac{\omega_c}{(\omega + i\tau^{-1})^2 - \omega_c^2}, \end{aligned} \quad (2)$$

where μ_c is the chemical potential (or Fermi level), ω is the photon frequency, $\tau = \mu \mu_c / e v_F^2$ is the intrinsic relaxation time (in graphene, the carrier mobility $\mu = 7000 \text{ cm}^2/\text{Vs}$, and Fermi velocity $v_F = 10^6 \text{ m/s}$), and $\omega_c = \frac{eB}{m^*} = eBv_F^2/\mu_c$

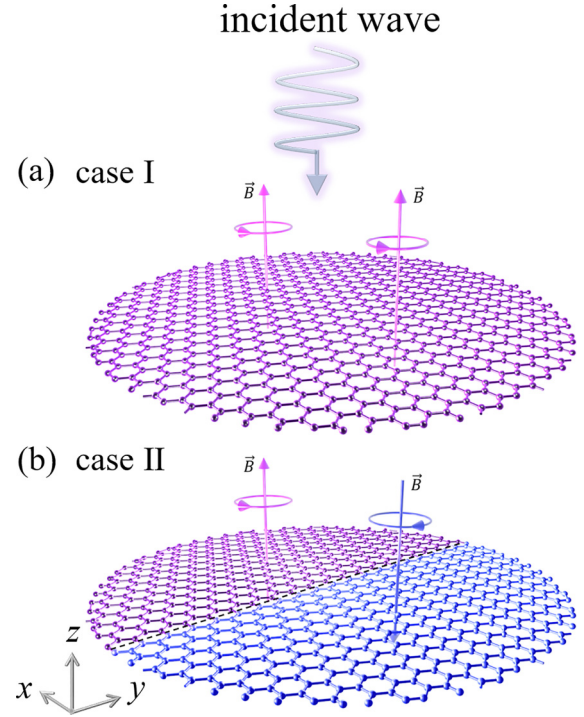


FIG. 1. Schematic diagrams of a graphene disk with its two halves in presence of either parallel (case I) or opposite (case II) magnetic fields. Magnitude of magnetic field is 5 T.

is the cyclotron resonance frequency. In graphene, to support specific plasmonic resonances, the chemical potential μ_c can be tuned dynamically via electrostatic gating, and the carrier mobility μ can be improved by using high-quality samples.

III. RESULTS AND DISCUSSION

We now study GMP excitations in graphene circular disks, as shown in Fig. 1, of which two halves are embedded in either parallel (case I) or antiparallel (case II) magnetic fields.

Case I is very common and easy to be achieved, while case II will be demonstrated later in this work. To characterize GMP splitting features, extinction cross section is employed, with full-wave simulation carried out by using a finite-element software package, COMSOL MULTIPHYSICS. In practice, graphene disk is placed in the center of a spherical computing domain, truncated by a perfectly matched layer. When a plane wave is normally incident with electric field in the xy plane, e.g., $\vec{E} = \vec{E}_0 e^{i(k_0 z - \omega t)}$, the normalized extinction cross section can be calculated by implementing the optical theorem, which can be written as [68,69]

$$\sigma_{\text{ext}} = \frac{4\pi}{Sk_0} \frac{\text{Im}\{\vec{E}_0^* \cdot \vec{F}(\vec{k} = k_0 \hat{z})\}}{|\vec{E}_0|^2}, \quad (3)$$

where S is the cross section of the disk, \vec{k} is the wave vector in free space, \vec{E}_0 is the incident amplitude, and $\vec{F}(\vec{k})$ is the scattering amplitude of the electric far field evaluated in the forward direction (along the incident wave vector), with its

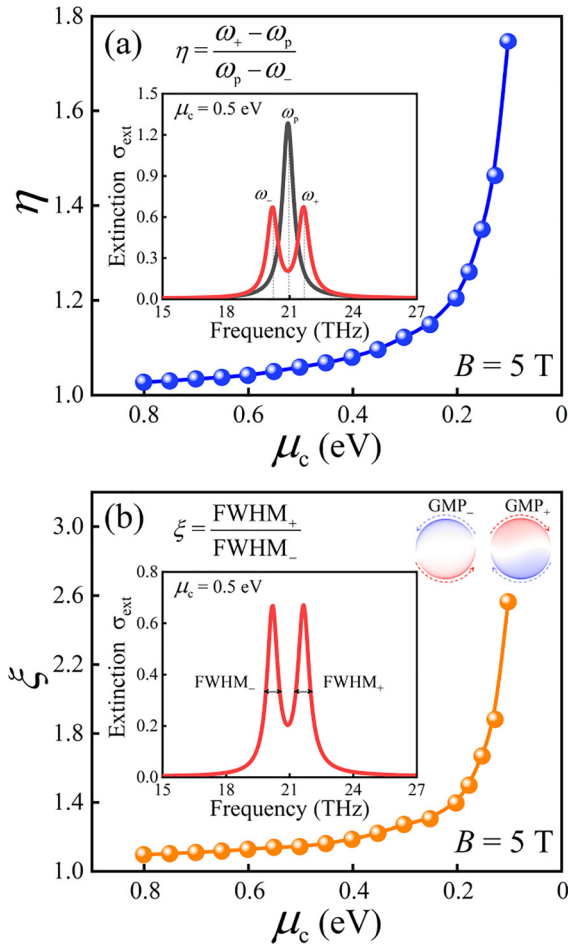


FIG. 2. Ratio of frequency difference η (a) and ratio of FWHM ξ (b) as function of chemical potential μ_c in case I. Insets show extinction spectra as magnetic field $B = 0$ T (black) and $B = 5$ T (red), and E_z field distributions, respectively. Dashed and horizontal lines mark extraction of resonance frequencies and FWHM, respectively.

component along the incident polarization vector extracted from the product $\vec{E}_0^* \cdot \vec{F}(k)$.

A. GMP excitations in case I

When the diameter of disk is 400 nm and magnetic field is 5 T (these values will be used throughout the work, except where noted), the results of case I are presented in Fig. 2. It is seen that as chemical potential $\mu_c = 0.5$ eV, two GMP peaks ω_+ and ω_- carrying LHCP and RHCP, respectively, exhibit a roughly symmetrical distribution with respect to plasmonic peak ω_p at zero magnetic field. Two GMPs are dipole states with angular momentum $l = 1$ (see field patterns), while the $l \neq 1$ states are not considered here since they are dark, e.g., embedded in extinction spectrum [66,70]. Such a symmetric mode splitting is well maintained with increasing μ_c , manifested itself as two peaks having the same frequency deviation and full width at half maximum (FWHM), namely, the ratios $\eta = (\omega_+ - \omega_p)/(\omega_p - \omega_-) \rightarrow 1$ and $\xi = \text{FWHM}_+/\text{FWHM}_- \rightarrow 1$. However, with decreasing μ_c , the two ratios will deviate from 1 gradually, and then rapidly as $\mu_c < 0.2$ eV, namely, the mode splitting of GMPs

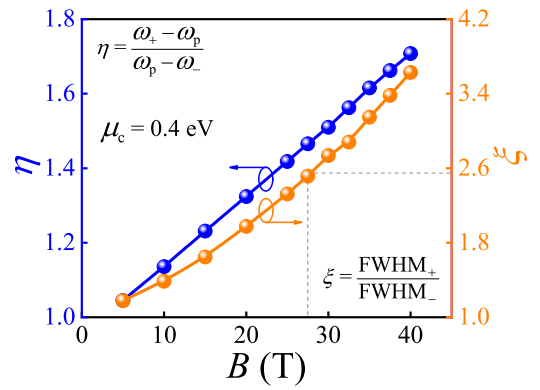


FIG. 3. Dependence of η and ξ on magnetic field B in case I as $\mu_c = 0.4$ eV. Dashed lines mark condition $\xi = 2.56$ at $B = 27.5$ T.

is not symmetric. This indicates the familiar symmetric mode splitting of GMPs actually depends on chemical potential, which only occurs for larger chemical potential. The variation of η can be predicted qualitatively by an empirical formula [57,71,72]:

$$\omega_{\pm} = \sqrt{\omega_p^2 + \frac{\omega_c^2}{4}} \pm \frac{\omega_c}{2}, \quad (4)$$

but quantitatively, a deviation will appear gradually as $\mu_c < 0.4$ eV, e.g., as $\mu_c = 0.1$ eV, $\eta = 1.75$ from simulation, while $\eta = 1.51$ from Eq. (4). More importantly, the variation of ξ goes beyond this formula. It is worth noting that as $\mu_c < 0.2$ eV, ξ can be larger than 2, which means FWHM of the lower-frequency GMP is significantly smaller than that of the higher-frequency GMP. In other words, the former has lower damping rate or higher quality factor (Q factor) than the latter. Taking into account their field patterns [see the insets in Fig. 2(b)], the former (left one) with field strongly bound to the edge, is usually classified as edge GMP [73–75]. It is easy to see that besides global frequency shift (similar to graphene plasmons), the active tunability of GMP enabled by external gating is also embodied in an essential change of GMP field profile.

As mentioned above, static magnetic field B acts as another degree of freedom for actively tuning GMP, which is clearly seen from Eq. (4). To study mode splitting here, a frequently used chemical potential $\mu_c = 0.4$ eV is chosen as a constant, and with increasing B , the simulation results are plotted in Fig. 3. Different from varying μ_c , both η and ξ increase roughly linearly, from 1.05 to 1.71 and from 1.18 to 3.63, respectively. This indicates the symmetric mode splitting will be broken for larger B , which thus can only survive for smaller B and larger μ_c (see Fig. 2). However, the effects of B and μ_c on mode splitting are different. As $\mu_c = 0.4$ eV and $B = 5$ T, the mode splitting is roughly symmetric, and then to achieve a narrow FWHM for edge GMP, e.g., $\xi = 2.56$, μ_c should be reduced to $1/4$ (0.1 eV, see Fig. 2), or B is increased to 5.5 times, namely, 27.5 T as indicated by the dashed lines. Clearly, μ_c provides a more efficient way to tune edge GMP, which could be understood by examining the competition between electric response (via ω_p) and magnetic response (via ω_c). To get a pronounced edge GMP, the former should be suppressed or the latter should be improved. According to the empirical

formula $\hbar\omega_p = e\sqrt{\mu_c/(\pi\epsilon_0 D)}$ (D the diameter of disk) [66] and $\omega_c = eBv_F^2/\mu_c$, with decreasing μ_c , ω_p and ω_c are decreased and increased, respectively, while with increasing B , only ω_c is increased. In addition, ω_p can also be decreased by adopting larger D , e.g., using micrometer disk, the effect of which could be quite similar to that with increasing B , so the relevant discussion will be omitted here. It is worth noting that ω_p can be further reduced as $\mu_c \ll 0.1$ eV, but then LLs will be resolved and a different conductivity formula should be adopted to replace the Drude formula [66].

Although characterized by η and ξ , the asymmetry of mode splitting can be considered as a direct consequence of the edge current formed by cyclotron motion of carriers, which is in the same (opposite) direction to ω_+ (ω_-) GMP, respectively. As compared to bulk current, the edge current suffers rather less scattering by defects and impurities. However, for larger μ_c and smaller B , e.g., $\omega_c \ll \omega_p$ in Eq. (4), the edge current will be mantled by the strong collective resonances, and results in a slight decrease (increase) of the period of ω_+ (ω_-) GMP, respectively. For smaller μ_c and larger B , ω_- GMP will be dominated by the edge current, which thus exhibits a narrower FWHM, while for ω_+ GMP, the edge current will merge into the bulk current, which causes a larger damping rate.

B. GMP excitations in case II

Different from case I, due to the antiparallel magnetic field the optical response of case II will be anisotropic, namely, the GMP excitations will be different, for incidence with electric field perpendicular and parallel to the border (y axis) marked by black dashed line in Fig. 1(b). The simulation results of the two polarizations are presented in Fig. 4. Impressively, there is no GMP mode splitting as shown by the inset of extinction spectrum in Fig. 4(a), which seems to be no magnetic field, e.g., the resonance curves of x (red) and y (blue) polarizations coincide exactly with that of zero magnetic field (black). At this moment, two identical resonance peaks are contributed by linear dipole states, rather than circularly polarized states in case I; see the insets GMP $_{\pm}$ in Fig. 4(a), with sign \pm for x and y polarization, respectively. It is clearly seen that despite the antiparallel magnetic field being distributed with no overlapping in space, the magnetic response is still canceled.

Since there is no mode splitting, the parameters η and ξ become ill defined, and for characterization they are redefined as $\eta = \omega_{\pm}/\omega_p$ and $\xi = \text{FWHM}_{\pm}/\text{FWHM}_p$. As shown in Fig. 4, for larger μ_c , e.g., $\mu_c \geq 0.45$ eV, η and ξ of two polarizations are equal to each other. With decreasing μ_c , those of x polarization will increase, while those of y polarization will decrease, as illustrated also by the inset of extinction spectrum in Fig. 4(b). The observation reveals the anisotropy of magnetoplasmonic excitation, which is quite different from the results of larger μ_c . More interestingly, a significant change occurs to GMP wave functions as well, which are again circularly polarized. However, different from case I, the fields bound to the edge (edge currents, equivalently) are circulating at each half, rather than forming a closed loop along the edge of the entire disk. It is also seen that with respect to the border (y axis) between antiparallel magnetic fields, GMP $_{\pm}$ are actually antisymmetric and symmetric mode, respectively, and as a clear difference, the current of

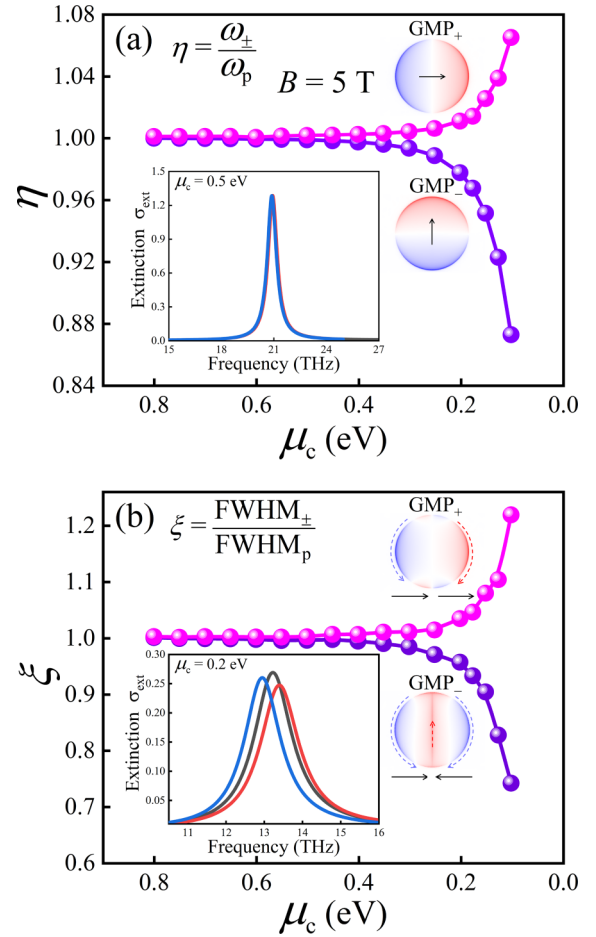


FIG. 4. Ratio of resonance frequency η (a) and ratio of FWHM ξ (b) as function of chemical potential μ_c in case II. Insets show extinction spectra and field patterns at $\mu_c = 0.5$ eV and $\mu_c = 0.2$ eV, respectively. Black, red, and blue curves represent spectra for $B = 0$ T, x , and y polarization, respectively.

GMP $_-$ is flowing along the border. Meanwhile, GMP $_{\pm}$ can be further interpreted as the superposition of two parallel dipoles and that of two antiparallel dipoles (marked by dark arrows), respectively.

C. Unidirectional field circulating of GMPs

Due to the dependence of GMP $_{\pm}$ on imposed magnetic field, especially the field of GMP $_-$ circulating along the magnetic border, it is certainly worth examining the evolution of GMP $_{\pm}$ as magnetic field at the right half changing gradually from +5 T (case I) to -5 T (case II). The simulation results are shown in Fig. 5. It is seen that with reducing magnetic field, e.g., deviating from case I, η and ξ of GMP $_{\pm}$ are approaching 1 (gray dashed lines), which means case I exhibits the largest asymmetric mode splitting, and a uniform magnetic field can help to form edge GMP $_-$ with low loss. With magnetic field at the right half $0 \leq B \leq 5$ T, Lorentz forces on carriers at the border from two magnetic fields are different in direction and magnitude, which can only cancel out as $B = 5$ T (e.g., case I). The remaining Lorentz force along + y direction will make the border an effective edge

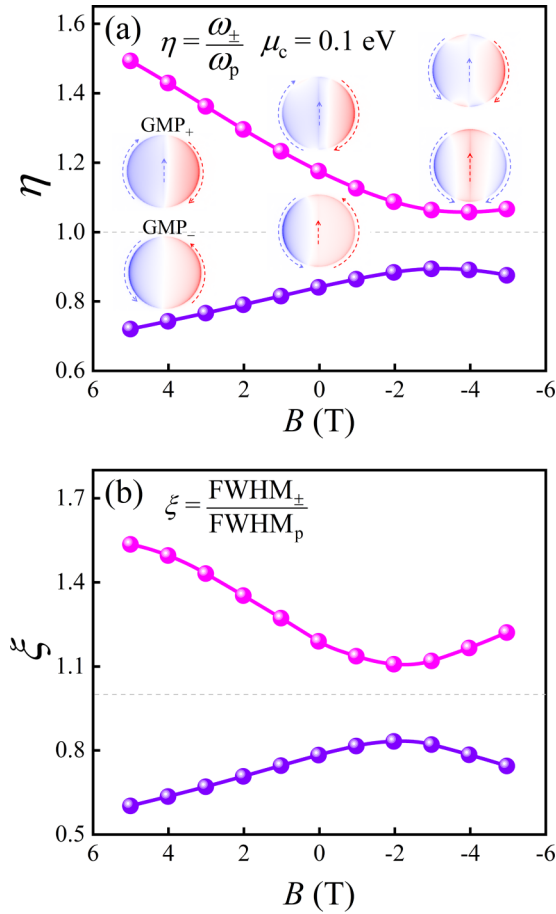


FIG. 5. Dependence of η and ξ on right magnetic field B in case II as $\mu_c = 0.1$ eV, while left magnetic field is constant 5 T. Insets show field patterns at $B = 4, 0$, and -4 T, respectively. Two dashed lines represent $\eta = 1$ and $\xi = 1$, respectively.

for GMP_{\pm} , and therefore induce circulating field along it (see insets). As $B < 0$ T, the two Lorentz forces are in the same direction, but contrary to GMP_- , the induced circulating fields of GMP_+ (antisymmetric mode) are out of phase, which results in a reduced and a zero circulating field along the border as $B \neq -5$ T and $B = -5$ T (case II), respectively.

As shown by the insets in Fig. 5, there is another interesting observation, namely, the circulating field always along $+y$ direction of the border. For conventional MPs in a uniform magnetic field, such as case I, their fields circulate clockwise or anticlockwise along the edge, corresponding to L/RHCP, respectively. This is a typical behavior of MPs, arising from the time-reverse symmetry breaking. If focusing on a specific segment of the edge, the field of one MP is circulating along one direction, while along the opposite direction for that of the other MP. As a pair of MPs, their resonance frequencies are different, and separated by ω_c . Thereby, at each resonance frequency of MPs, the field is circulating unidirectionally. Although local states, this feature of MPs can be employed to engineer unidirectional propagation by arranging an array of these MP resonators [76–78]. The key point is to move backscattering out of the operating frequency region. However, by applying nonuniform magnetic fields, as shown in Fig. 5, the fields circulating along the border are in the same

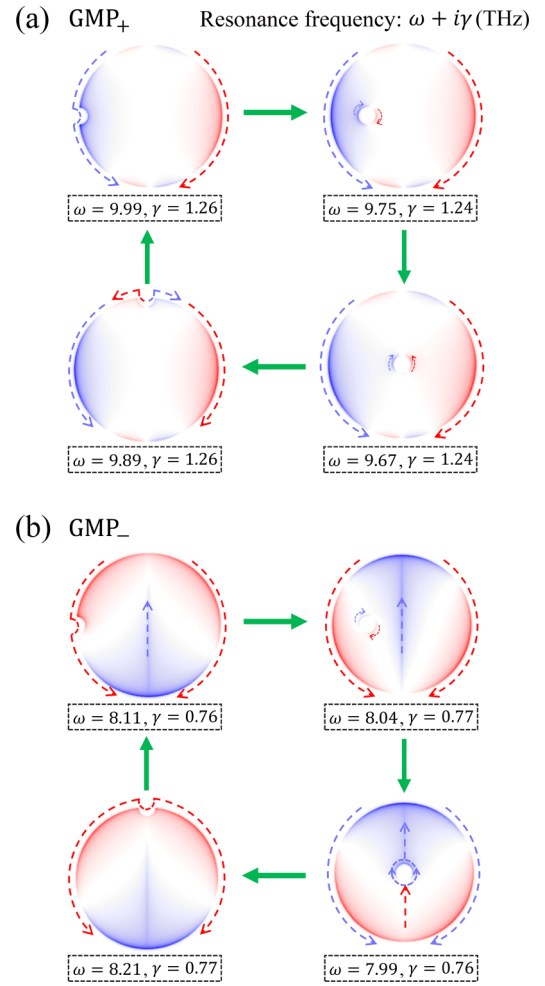


FIG. 6. Field circulating of GMP_+ (a) and GMP_- (b) in presence of small defect at different positions.

direction for the pair of MPs, namely, GMP_{\pm} , while in case II, the field circulating along the border is only contributed by GMP_- . It is clear that as the right magnetic field $-5 \text{ T} \leq B \leq 5 \text{ T}$, backscattering is always absent naturally, and the change of B only results in different strength of circulating field. To reverse the field circulating, the left and right magnetic fields should be exchanged. Thus, the unidirectional field circulating of GMP_{\pm} is rather robust, which makes them excellent candidates for device applications.

Besides magnetic fields, the unidirectional field circulating of GMP_{\pm} is also immune to small defects. To illustrate this, a circular hole of diameter 25 nm is introduced and then placed at four different positions. Taking case II for example, there are no additional modes circulating along the border, and the circulating direction of GMP_{\pm} is well maintained. As shown in Fig. 6(a), in four cases the antisymmetric field circulating of GMP_+ remains, and the field circulating is always canceled at the magnetic border. It means the defect scattering will not change the circulating feature of GMP_+ . For GMP_- [Fig. 6(b)], the field circulating is symmetric and along $+y$ direction of the magnetic border in four cases. There is no backscattering caused by the hole, which only results in a slight change of resonance frequency, mostly its real part.

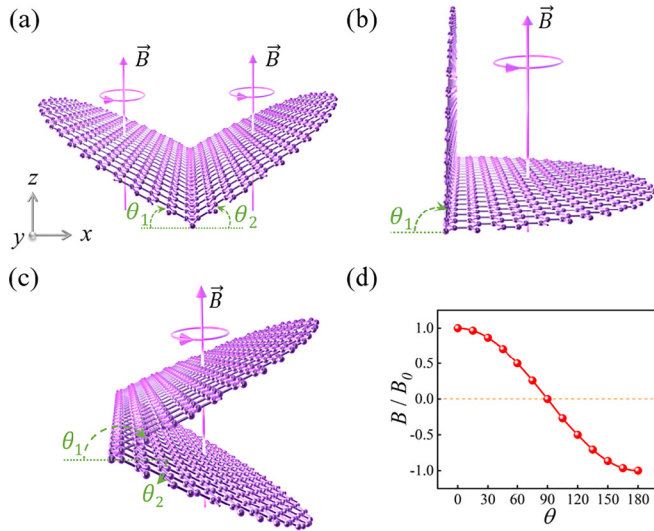


FIG. 7. (a), (b), and (c) three different folding procedures with folding axis along y direction and in uniform magnetic field $B = B_0$. (d) Dependence of effective magnetic field on folding angle θ .

Even with the hole across the border, the circulating field can pass around it smoothly.

D. Tunable magnetic field distributions by folding

To achieve unidirectional field circulating of GMP_{\pm} along the border, nonuniform magnetic field distribution is crucial, e.g., case II and the situations studied in Fig. 5. Since magnetic field changes its magnitude and/or direction over hundreds of nanometers, it may be difficult to be implemented practically. This issue can be solved by employing a recently developed technique, namely, graphene folding, also known as graphene origami [79–81], which in particular has been demonstrated to be atomically precise and custom designed via a scanning tunneling microscope (STM) tip [82]. Folding is emerging as a new degree of freedom for graphene plasmonics [83–85]. For GMPs, graphene folding is even more efficient, through which two halves of a planar graphene disk can have different angles with magnetic field, thus producing different effective perpendicular magnetic fields.

Supposing a planar graphene disk placed in xy plane and a uniform magnetic field B_0 along $+z$ direction, e.g., case I, the effective magnetic fields on two halves can be tuned via graphene folding along an arbitrary axis. Due to the rotational symmetry, it is sufficient to study the case as axis along the y direction. As shown in Fig. 7, different folding procedures will produce different magnetic field distributions. It is seen that if two halves are folded to $+z$ direction with angles θ_1 and θ_2 , respectively, both of them will experience positive magnetic fields, yet with different magnitudes [Fig. 7(a)]. As a special case $0 \leq \theta_1 < 180^\circ$ and $\theta_2 = 0$, magnetic fields on the left and right halves are $-B_0 < B \leq B_0$ and $B = B_0$, respectively, and then as $\theta_1 = 90^\circ$ [Fig. 7(b)], magnetic field on the left half will be zero. On the other hand, the two halves can be folded to $+z$ and $-z$ direction, respectively. As $90^\circ < \theta_1 < 180^\circ$ and $0 < \theta_2 < 90^\circ$ [Fig. 7(c)], the two effective magnetic fields are always opposite in direction, and if $\theta_1 + \theta_2 = 180^\circ$,

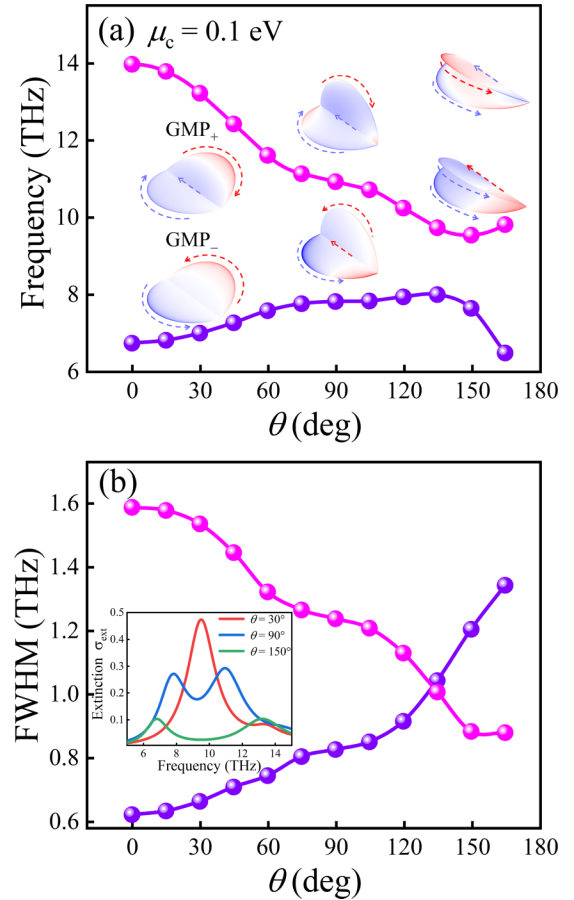


FIG. 8. Resonance frequency and FWHM of GMP_{\pm} in folded graphene disks as function of folding angle θ . Insets show field patterns and extinction spectra, respectively.

they will be equal in magnitude, such as case II. Generally, the magnetic field on the folded halves with folding angle θ is given by a simple cosine function, e.g., $B = B_0 \cos \theta$, of which the evolution is shown in Fig. 7(d). It is clear that by means of folding, magnetic field distributions mentioned above can be realized.

Through folding, the required magnetic field distributions can be obtained, but as compared to a planar graphene disk, the structures are changed as well, especially the interactions between two halves. Hence, it is worth to confirm those interesting features of GMP_{\pm} in such systems. Without loss of generality, the folding in Fig. 7(b) is taken as an example. Similarly, GMP_{\pm} are extracted from extinction spectra of y polarization [inset in Fig. 8(b)]. The simulation results are shown in Fig. 8. It is seen that with increasing θ (decreasing B , equivalently), the resonance frequency and FWHM of GMP_{\pm} exhibit a gradual decrease and increase, respectively, which follow similar change rules as those in Fig. 5. The differences at larger θ , e.g., the cross of FWHM, might come from the strong interactions between two halves. Most importantly, the field patterns of GMP_{\pm} and their circulating along the border [insets in Fig. 8(a)] are well maintained, which directly verify the feasibility of the proposed scheme.

It is worth noting that the studied graphene structures, e.g., disks and folded disks, are very common in many other works.

The fabrication of these structures has been well developed. High-quality monolayer graphene can be grown on copper foil by using an optimized chemical vapor deposition method [86], and can be identified by Raman spectroscopy [87]. Then, graphene is transferred onto a resistive silicon substrate with a thermal oxide layer, and is further patterned into disks via standard electron-beam lithography and plasma etching. The disks are fabricated with diameter from tens of nanometers [20] to a few micrometers [57]. To proceed folding, graphene will be transferred to a tailed substrate having a hydrophobic region and a hydrophilic region, and when immersed in water, film delamination from the hydrophilic region is controlled to achieve folding [79]. Meanwhile, surface functionalization of graphene using particular polymers with water absorption [80] or thermoresponsive properties [81] were reported to produce folding, and more complicated structures, e.g., box and flower, were obtained. Furthermore, mechanical scheme can also be implemented to fold graphene in an ultrahigh vacuum, low-temperature STM system such as place the STM tip close to the edge of graphene, reduce the resistance in the STM tunneling junction to lift graphene by the edge, and move the tip along a predefined route [82].

IV. CONCLUSION

To summarize, we theoretically study GMPs in graphene disks in the presence of different static magnetic fields. We show that in a uniform magnetic field (case I, a common scenario), the well-known symmetric mode splitting of MPs is actually dependent on chemical potential μ_c , which will be broken with decreasing μ_c . The resulting MPs of R/LHCP,

GMP $_{\pm}$, exhibit the resonance features of bulk and edge states, e.g., the lower-energy GMP $_{-}$ is bound to the edge, with a strongly suppressed damping rate. In antisymmetric magnetic fields (case II), there is an effective border along the diameter, and for larger μ_c , the extinction spectra of two polarizations (electric field parallel and perpendicular to the border) are identical, with only one peak, at which GMP $_{\pm}$ are degenerate and linearly polarized. This indicates the cancellation of magnetic effects. However, with decreasing μ_c , GMP $_{\pm}$ will differ in energy and damping rate, which increase and decrease, respectively, and moreover, they are circularly polarized again. Regarding GMP $_{-}$, its field will be circulating unidirectionally along the border. With magnetic field distribution changing gradually from case I to case II, it is found that both GMP $_{\pm}$ manifest field circulating along the border, interestingly, in the same direction. Furthermore, even in the presence of a defect at arbitrary positions, the opposite field circulating along the border will be prohibited, which implies the robust feature of unidirectional field circulating of GMP $_{\pm}$. Finally, we propose a feasible scheme to achieve concerned magnetic field distributions, namely, by means of mechanical folding, and the features of GMP $_{\pm}$, especially unidirectional field circulating, are seen to be well maintained. Our findings present some important features of MPs, which could pave the way for advanced magneto-optic devices.

ACKNOWLEDGMENT

This work is supported by the National Natural Science Foundation of China (NSFC) (Grant No. 12174440).

-
- [1] D. K. Gramotnev and S. I. Bozhevolnyi, *Nat. Photon.* **4**, 83 (2010).
- [2] S. Kawata, Y. Inouye, and P. Verma, *Nat. Photon.* **3**, 388 (2009).
- [3] R. F. Oulton, V. J. Sorger, T. Zentgraf, R.-M. Ma, C. Gladden, L. Dai, G. Bartal, and X. Zhang, *Nature (London)* **461**, 629 (2009).
- [4] J. A. Schuller, E. S. Barnard, W. Cai, Y. C. Jun, J. S. White, and M. L. Brongersma, *Nat. Mater.* **9**, 193 (2010).
- [5] W. L. Barnes, A. Dereux, and T. W. Ebbesen, *Nature (London)* **424**, 824 (2003).
- [6] E. Ozbay, *Science* **311**, 189 (2006).
- [7] K. S. Novoselov, A. K. Geim, S. V. Morozov, D. Jiang, Y. Zhang, S. V. Dubonos, I. V. Grigorieva, and A. A. Firsov, *Science* **306**, 666 (2004).
- [8] A. K. Geim and K. S. Novoselov, *Nat. Mater.* **6**, 183 (2007).
- [9] F. H. L. Koppens, D. E. Chang, and F. J. G. de Abajo, *Nano Lett.* **11**, 3370 (2011).
- [10] F. J. Garcia de Abajo, *ACS Photon.* **1**, 135 (2014).
- [11] J. Christensen, A. Manjavacas, S. Thongrattanasiri, F. H. L. Koppens, and F. J. G. de Abajo, *ACS Nano* **6**, 431 (2012).
- [12] G. X. Ni, L. Wang, M. D. Goldflam, M. Wagner, Z. Fei, A. S. McLeod, M. K. Liu, F. Keilmann, B. Özyilmaz, and A. H. C. Neto, *Nat. Photon.* **10**, 244 (2016).
- [13] A. Woessner, M. B. Lundeberg, Y. Gao, A. Principi, P. Alonso-González, M. Carrega, K. Watanabe, T. Taniguchi, G. Vignale, M. Polini *et al.*, *Nat. Mater.* **14**, 421 (2015).
- [14] A. Principi, M. Carrega, M. B. Lundeberg, A. Woessner, F. H. L. Koppens, G. Vignale, and M. Polini, *Phys. Rev. B* **90**, 165408 (2014).
- [15] Z. Fei, A. S. Rodin, G. O. Andreev, W. Bao, A. S. McLeod, M. Wagner, L. M. Zhang, Z. Zhao, M. Thiemens, G. Dominguez, M. M. Fogler, A. H. Castro Neto, C. N. Lau, F. Keilmann, and D. N. Basov, *Nature (London)* **487**, 82 (2012).
- [16] T. Low and P. Avouris, *ACS Nano* **8**, 1086 (2014).
- [17] L. Ju, B. Geng, J. Horng, C. Girit, M. Martin, Z. Hao, H. A. Bechtel, X. Liang, A. Zettl, and Y. R. Shen, *Nat. Nanotechnol.* **6**, 630 (2011).
- [18] M. Jablan, H. Buljan, and M. Soljačić, *Phys. Rev. B* **80**, 245435 (2009).
- [19] F. Wang, Y. Zhang, C. Tian, C. Girit, A. Zettl, M. Crommie, and Y. R. Shen, *Science* **320**, 206 (2008).
- [20] Z. Fang, S. Thongrattanasiri, A. Schlather, Z. Liu, L. Ma, Y. Wang, P. M. Ajayan, P. Nordlander, N. J. Halas, and F. J. G. de Abajo, *ACS Nano* **7**, 2388 (2013).
- [21] K. S. Novoselov, A. K. Geim, S. V. Morozov, D. Jiang, M. I. Katsnelson, I. V. Grigorieva, S. V. Dubonos, and A. A. Firsov, *Nature (London)* **438**, 197 (2005).
- [22] P. Avouris, *Nano Lett.* **10**, 4285 (2010).
- [23] A. H. Castro Neto, F. Guinea, N. M. R. Peres, K. S. Novoselov, and A. K. Geim, *Rev. Mod. Phys.* **81**, 109 (2009).
- [24] S. Thongrattanasiri and F. J. García de Abajo, *Phys. Rev. Lett.* **110**, 187401 (2013).

- [25] N. A. Mortensen, S. Raza, M. Wubs, T. Søndergaard, and S. I. Bozhevolnyi, *Nat. Commun.* **5**, 3809 (2014).
- [26] E. J. C. Dias, D. A. Iranzo, P. A. D. Gonçalves, Y. Hajati, Y. V. Bludov, A.-P. Jauho, N. A. Mortensen, F. H. L. Koppens, and N. M. R. Peres, *Phys. Rev. B* **97**, 245405 (2018).
- [27] M. Gullans, D. E. Chang, F. H. L. Koppens, F. J. García de Abajo, and M. D. Lukin, *Phys. Rev. Lett.* **111**, 247401 (2013).
- [28] F. Karimi, A. H. Davoody, and I. Knezevic, *Phys. Rev. B* **97**, 245403 (2018).
- [29] T. Christensen, W. Yan, A.-P. Jauho, M. Wubs, and N. A. Mortensen, *Phys. Rev. B* **92**, 121407 (2015).
- [30] M. Jablan and D. E. Chang, *Phys. Rev. Lett.* **114**, 236801 (2015).
- [31] S. Thongrattanasiri, A. Manjavacas, and F. J. García de Abajo, *ACS Nano* **6**, 1766 (2012).
- [32] J. D. Cox, I. Silveiro, and F. J. García de Abajo, *ACS Nano* **10**, 1995 (2016).
- [33] K. S. Novoselov, Z. Jiang, Y. Zhang, S. V. Morozov, H. L. Stormer, U. Zeitler, J. C. Maan, G. S. Boebinger, P. Kim, and A. K. Geim, *Science* **315**, 1379 (2007).
- [34] S. Murakami, N. Nagaosa, and S.-C. Zhang, *Science* **301**, 1348 (2003).
- [35] F. Guinea, M. I. Katsnelson, and A. K. Geim, *Nat. Phys.* **6**, 30 (2010).
- [36] Y. Zhang, Z. Jiang, J. P. Small, M. S. Purewal, Y.-W. Tan, M. Fazlollahi, J. D. Chudow, J. A. Jaszczak, H. L. Stormer, and P. Kim, *Phys. Rev. Lett.* **96**, 136806 (2006).
- [37] M. R. Peterson and C. Nayak, *Phys. Rev. Lett.* **113**, 086401 (2014).
- [38] Y.-H. Zhang, H. C. Po, and T. Senthil, *Phys. Rev. B* **100**, 125104 (2019).
- [39] G. Armelles, A. Cebollada, A. García-Martín, and M. U. González, *Adv. Opt. Mater.* **1**, 10 (2013).
- [40] D. Floess and H. Giessen, *Rep. Prog. Phys.* **81**, 116401 (2018).
- [41] B. Hu, Y. Zhang, and Q. J. Wang, *Nanophotonics* **4**, 383 (2015).
- [42] I. Crassee, J. Levallois, A. L. Walter, M. Ostler, A. Bostwick, E. Rotenberg, T. Seyller, D. Van Der Marel, and A. B. Kuzmenko, *Nat. Phys.* **7**, 48 (2011).
- [43] M. Tymchenko, A. Yu. Nikitin, and L. Martín-Moreno, *ACS Nano* **7**, 9780 (2013).
- [44] D. Jin, T. Christensen, M. Soljačić, N. X. Fang, L. Lu, and X. Zhang, *Phys. Rev. Lett.* **118**, 245301 (2017).
- [45] D. Jin, L. Lu, Z. Wang, C. Fang, J. D. Joannopoulos, M. Soljačić, L. Fu, and N. X. Fang, *Nat. Commun.* **7**, 13486 (2016).
- [46] C. Finnigan, M. Kargarian, and D. K. Efimkin, *Phys. Rev. B* **105**, 205426 (2022).
- [47] D. Pan, R. Yu, H. Xu, and F. J. García de Abajo, *Nat. Commun.* **8**, 1243 (2017).
- [48] D. Jin, Y. Xia, T. Christensen, M. Freeman, S. Wang, K. Y. Fong, G. C. Gardner, S. Fallahi, Q. Hu, Y. Wang, L. Engel, Z.-L. Xiao, M. J. Manfra, N. X. Fang, and X. Zhang, *Nat. Commun.* **10**, 4565 (2019).
- [49] D. A. Kuzmin, I. V. Bychkov, V. G. Shavrov, and V. V. Temnov, *Nanophotonics* **7**, 597 (2018).
- [50] M. Tamagnone, C. Moldovan, J.-M. Pomirol, A. B. Kuzmenko, A. M. Ionescu, J. R. Mosig, and J. Perruisseau-Carrier, *Nat. Commun.* **7**, 11216 (2016).
- [51] W. Wu, S. Chen, C. Mi, W. Zhang, H. Luo, and S. Wen, *Phys. Rev. A* **96**, 043814 (2017).
- [52] R. Shimano, G. Yumoto, J. Y. Yoo, R. Matsunaga, S. Tanabe, H. Hibino, T. Morimoto, and H. Aoki, *Nat. Commun.* **4**, 1841 (2013).
- [53] T. Tang, J. Li, L. Luo, P. Sun, and J. Yao, *Adv. Opt. Mater.* **6**, 1701212 (2018).
- [54] N. Jiao, S. Kang, K. Han, X. Shen, and W. Wang, *Phys. Rev. B* **99**, 195447 (2019).
- [55] N. Jiao, S. Kang, K. Han, X. Shen, and W. Wang, *Phys. Rev. B* **103**, 085405 (2021).
- [56] N. Wang, L. Ding, and W. Wang, *Phys. Rev. B* **105**, 235435 (2022).
- [57] H. Yan, Z. Li, X. Li, W. Zhu, P. Avouris, and F. Xia, *Nano Lett.* **12**, 3766 (2012).
- [58] I. Crassee, M. Orlita, M. Potemski, A. L. Walter, M. Ostler, Th. Seyller, I. Gaponenko, J. Chen, and A. B. Kuzmenko, *Nano Lett.* **12**, 2470 (2012).
- [59] N. Kumada, S. Tanabe, H. Hibino, H. Kamata, M. Hashisaka, K. Muraki, and T. Fujisawa, *Nat. Commun.* **4**, 1363 (2012).
- [60] P. B. Johnson and R. W. Christy, *Phys. Rev. B* **6**, 4370 (1972).
- [61] M. Scheffler, M. Dressel, M. Jourdan, and H. Adrian, *Nature (London)* **438**, 1135 (2005).
- [62] R. L. Olmon, B. Slovick, T. W. Johnson, D. Shelton, S.-H. Oh, G. D. Boreman, and M. B. Raschke, *Phys. Rev. B* **86**, 235147 (2012).
- [63] T. Kawarabayashi, Y. Hatsugai, and H. Aoki, *Phys. Rev. B* **85**, 165410 (2012).
- [64] A. D. Güçlü, P. Potasz, and P. Hawrylak, *Phys. Rev. B* **88**, 155429 (2013).
- [65] M. I. Katsnelson and M. F. Prokhorova, *Phys. Rev. B* **77**, 205424 (2008).
- [66] W. Wang, S. P. Apell, and J. M. Kinaret, *Phys. Rev. B* **86**, 125450 (2012).
- [67] C. H. Yang, F. M. Peeters, and W. Xu, *Phys. Rev. B* **82**, 205428 (2010).
- [68] A. B. Evlyukhin, T. Fischer, C. Reinhardt, and B. N. Chichkov, *Phys. Rev. B* **94**, 205434 (2016).
- [69] M. J. Berg, C. M. Sorensen, and A. Chakrabarti, *J. Opt. Soc. Am. A* **25**, 1504 (2008).
- [70] W. Wang, P. Apell, and J. Kinaret, *Phys. Rev. B* **84**, 085423 (2011).
- [71] S. J. Allen, H. L. Stormer, and J. C. M. Hwang, *Phys. Rev. B* **28**, 4875 (1983).
- [72] R. P. Leavitt and J. W. Little, *Phys. Rev. B* **34**, 2450 (1986).
- [73] W. Wang, J. M. Kinaret, and S. P. Apell, *Phys. Rev. B* **85**, 235444 (2012).
- [74] A. A. Sokolik and Y. E. Lozovik, *Phys. Rev. B* **100**, 125409 (2019).
- [75] N. Kumada, H. Kamata, and T. Fujisawa, *Phys. Rev. B* **84**, 045314 (2011).
- [76] Z. Yu, G. Veronis, Z. Wang, and S. Fan, *Phys. Rev. Lett.* **100**, 023902 (2008).
- [77] K. Liu, A. Torki, and S. He, *Opt. Lett.* **41**, 800 (2016).
- [78] B. Hu, Q. J. Wang, and Y. Zhang, *Opt. Lett.* **37**, 1895 (2012).
- [79] B. Wang, M. Huang, N. Y. Kim, B. V. Cunniff, Y. Huang, D. Qu, X. Chen, S. Jin, M. Biswal, X. Zhang, S. H. Lee, H. Lim, W. J. Yoo, Z. Lee, and R. S. Ruoff, *Nano Lett.* **17**, 1467 (2017).
- [80] J. Mu, C. Hou, H. Wang, Y. Li, Q. Zhang, and M. Zhu, *Sci. Adv.* **1**, e1500533 (2015).
- [81] W. Xu, Z. Qin, C.-T. Chen, H. R. Kwag, Q. Ma, A. Sarkar, M. J. Buehler, and D. H. Gracias, *Sci. Adv.* **3**, e1701084 (2017).

- [82] H. Chen, X.-L. Zhang, Y.-Y. Zhang, D. Wang, D.-L. Bao, Y. Que, W. Xiao, S. Du, M. Ouyang, S. T. Pantelides, and H.-J. Gao, *Science* **365**, 1036 (2019).
- [83] R. Zhang, S. Wang, B. You, K. Han, X. Shen, and W. Wang, *J. Opt.* **23**, 025001 (2021).
- [84] W. Wang and R. Zhang, *J. Opt.* **24**, 085001 (2022).
- [85] R. Zhang and W. Wang, *Opt. Express*, **30**, 44726 (2022).
- [86] X. Li, W. Cai, J. An, S. Kim, J. Nah, D. Yang, R. Piner, A. Velamakanni, I. Jung, E. Tutuc, S. K. Banerjee, L. Colombo, and R. S. Ruoff, *Science* **324**, 1312 (2009).
- [87] A. C. Ferrari, J. C. Meyer, V. Scardaci, C. Casiraghi, M. Lazzeri, F. Mauri, S. Piscanec, D. Jiang, K. S. Novoselov, S. Roth, and A. K. Geim, *Phys. Rev. Lett.* **97**, 187401 (2006).